
CHAPTER 10

Analysis of Microtubule Curvature

Andrew D. Bicek,[★] Erkan Tüzel,^{†,‡} Daniel M. Kroll,[§] and David J. Odde[★]

[★]Department of Biomedical Engineering
University of Minnesota
Minneapolis, Minnesota 55455

[†]School of Physics and Astronomy
University of Minnesota
Minneapolis, Minnesota 55455

[‡]Supercomputing Institute
University of Minnesota
Minneapolis, Minnesota 55455

[§]Department of Physics
North Dakota State University
Fargo, North Dakota 58105

Abstract

- I. Introduction
- II. Rationale
- III. Raw Data Collection
 - A. Point-Click Method
 - B. Semiautomated Methods
 - C. Data Collection Errors
- IV. Validation Strategy
 - A. Modeling of Semiflexible Polymers
 - B. Generation of Simulated Data
 - C. Validation of Semiflexible Polymer Simulation
- V. Curvature Estimation Methods
 - A. Three-Point Method
 - B. Shape-Fitting Method
 - C. Constructing the Curvature Distribution
- VI. Results
 - A. Three-Point Method
 - B. Shape-Fitting Method

VII.	Discussion
VIII.	Conclusions
	References

Abstract

The microtubule cytoskeleton in living cells generate and resist mechanical forces to mediate fundamental cell processes, including cell division and migration. Recent advances in digital fluorescence microscopy have enabled the direct observation of bending of individual microtubules in living cells, which has enabled quantitative estimation of the mechanical state of the microtubule array. Although a variety of mechanisms have been proposed, the precise origins of microtubule deformation in living cells remain largely obscure. To investigate these mechanisms and their relative importance in cellular processes, a method is needed to accurately quantify microtubule bending within living cells. Here we describe a method for quantification of bending, using digital fluorescence microscope images to estimate the distribution of curvature in the microtubule. Digital images of individual microtubules can be used to obtain a set of discrete x - y coordinates along the microtubule contour, which is then used to estimate the curvature distribution. Due to system noise and digitization error, the estimate will be inaccurate to some degree. To quantify the inaccuracy, a computational model is used to simulate both the bending of thermally driven microtubules and their observation by digital fluorescence microscopy. This allows for direct comparison between experimental and simulated images, a method which we call model convolution microscopy. We assess the accuracy of various methods and present a suitable method for estimating the curvature distribution for thermally driven semiflexible polymers. Finally, we discuss extensions of the method to quantify microtubule curvature in living cells.

I. Introduction

Living cells respond to mechanical signals from their environment. A potential cellular-based sensory apparatus for mechanical signal transduction is the cytoskeleton, a filamentous network composed of microtubules, actin filaments, and intermediate filaments. Together, these structures provide shape and mechanical integrity for the cell. In addition, they mediate motor-based transport of membrane-bound organelles and vesicles, generate force for cell locomotion, and are essential for cell division. Since force is generated within the cytoskeleton via molecular motors and can be locally accommodated and dissipated ([Brangwynne *et al.*, 2006](#); [Heidemann *et al.*, 1999](#); [Odde *et al.*, 1999](#); [Waterman-Storer and Salmon, 1997](#)), the cytoskeleton may act as a mechanosensitive element by responding to force ([Putnam *et al.*, 1998](#)). Therefore, by measuring the characteristic shapes of cytoskeletal structures in the cell and comparing, if possible, to

in vitro shapes of the isolated structures, it may be possible to gain insight into the intracellular mechanical stresses.

One type of cytoskeletal filament in particular, the microtubule, is believed to be important for vesicle trafficking and transport, organelle positioning, chromosome segregation, and cell shape and integrity. Because of its resistance to bending and deformation under compressive loads, an analysis of microtubule shape holds promise for force determinations. Microtubules are linear polymers composed of the $\alpha\beta$ -heterodimeric protein tubulin, which assembles head-to-tail to form a protofilament. In a typical microtubule, there are 13 protofilaments that form a tube of 25-nm outer diameter and 16-nm inner diameter ([Desai and Mitchison, 1997](#)). The tubular structure increases the second moment of the cross-sectional area (I ; a measure of the distribution of mass relative to the centroid of the cross section) compared to a solid rod of the same mass, thereby increasing its resistance to bending from external forces. The flexural rigidity, EI , (elastic modulus multiplied by the second moment of the cross-sectional area) of microtubules has been estimated *in vitro*, and the reported values range from $1 \times 10^{-24} \text{ N m}^2$ to $200 \times 10^{-24} \text{ N m}^2$ ($1\text{--}200 \text{ pN } \mu\text{m}^2$) depending on the experimental conditions and the measurement technique ([Cassimeris et al., 2001](#); [Felgner et al., 1997, 1996](#); [Fygenson et al., 1997](#); [Gittes et al., 1993](#); [Janson and Dogterom, 2004](#); [Kis et al., 2002](#); [Kurachi et al., 1995](#); [Kurz and Williams, 1995](#); [Mickey and Howard, 1995](#); [Takasone et al., 2002](#); [Venier et al., 1994](#)). Assuming that the microtubule is an isotropic solid continuum, I (second moment of the cross-sectional area) is estimated to be on the order of 10^{-32} m^4 based on the known dimension of the tubular structures, and thus the elastic modulus is approximately $E \cong 1 \times 10^9 \text{ Pa}$, which is similar to Plexiglas® and indicates that microtubules are indeed stiff filaments.

Dynamic microtubules observed *in vivo* often stochastically switch between alternate states of roughly constant growth and shortening, a phenomenon known as dynamic instability ([Desai and Mitchison, 1997](#); [Mitchison and Kirschner, 1984](#)). Dynamic instability presumably allows microtubules to rapidly explore a variety of arrangements within the cytoplasm, with preferred spatial arrangements arising via spatially selective protection of microtubules against depolymerization ([Kirschner and Mitchison, 1986](#)). Understanding the mechanisms that provide spatially selective stabilization of microtubules is a key issue in understanding cell polarization. In particular, previous studies have focused largely on the chemical origin of microtubule-stabilization as mediated by microtubule-associated proteins, but recent studies also point to a significant mechanical basis of stabilization, where compressive forces acting on microtubules *in vitro* slow microtubule assembly and promote catastrophe, the abrupt transition from growing to shortening ([Dogterom and Yurke, 1997](#); [Janson and Dogterom, 2004](#); [Janson et al., 2003](#)). Conversely, stretching forces applied to living cells have been found to induce microtubule extension ([Zheng et al., 1993](#); [Kaverina et al., 2002](#); [Putnam et al., 1998](#)).

The extent to which compressive forces play a role in controlling microtubule assembly *in vivo* is unclear, but it is clear that microtubules are under mechanical

stress, as evidenced by the direct observation of the curving of individual fluorescently tagged microtubules in living cells. Much like classical rods and tubes in macroscopic structures, microtubules are capable of bending and breaking ([Gupton *et al.*, 2002](#); [Odde *et al.*, 1999](#); [Waterman-Storer and Salmon, 1997](#)). Bending enables the relatively stiff microtubules to store elastic strain energy. This is evident in cilia and flagella, where the energy from the bent microtubule is used to propel the cell relative to the surrounding fluid. In addition, microtubule bending could more generally affect microtubule dynamic instability, and thereby change the microtubule organization within the cell. By increasing the elastic strain energy through bending, the growth and shortening dynamics of the microtubule may be altered, thereby creating a mechanical mechanism that is capable of regulating and reorganizing the microtubule network over time ([Odde *et al.*, 1999](#)). In addition, microtubule breaking exposes the labile core of microtubules, which tends to promote disassembly from the site of breaking ([Odde *et al.*, 1999](#); [Waterman-Storer and Salmon, 1997](#)).

II. Rationale

Microtubule bending is commonly observed in fluorescent images of microtubules *in vivo*; however, the mechanisms which cause microtubule bending are still largely unknown. Specific sources of bending have been identified, including thermal forces ([Cassimeris *et al.*, 2001](#); [Gittes *et al.*, 1993](#); [Kurz and Williams, 1995](#); [Mickey and Howard, 1995](#); [Venier *et al.*, 1994](#)), microtubule polymerization ([Dogterom and Yurke, 1997](#); [Janson and Dogterom, 2004](#); [Janson *et al.*, 2003](#)), and actomyosin contractility ([Gupton *et al.*, 2002](#); [Waterman-Storer and Salmon, 1997](#)). The extent to which these mechanisms contribute to the deformation of microtubules in living cells is still largely unknown. In addition, analysis of microtubule bending may serve as a useful tool for measuring net mechanical stress in different regions of a cell.

A number of groups have investigated the mapping of microtubules, actin filaments, and DNA shapes into discrete x - y coordinates in order to estimate the flexural rigidity ([Gittes *et al.*, 1993](#); [Janson and Dogterom, 2004](#); [Kurz and Williams, 1995](#); [Ott *et al.*, 1993](#); [Venier *et al.*, 1994](#)) and microtubule curvature *in vivo* ([Odde *et al.*, 1999](#)). While the analysis techniques vary, the underlying data collection techniques are similar in that they first require collection of digitized x - y coordinates from a raw image as the initial step, followed by estimation of the mechanical deformation.

The resistance to microtubule bending is characterized by the flexural rigidity, which is both a material and geometrical property of the microtubule. There are many ways to estimate EI , but it is essential to know the manner in which the forces are applied in order to make an accurate estimate. One approach is to simply exploit thermal forces and measure quantities such as end fluctuations ([Cassimeris *et al.*, 2001](#)), end-to-end fluctuations ([Van Noort *et al.*, 2003](#)), shape fluctuations

(Gittes *et al.*, 1993; Kurz and Williams, 1995; Mickey and Howard, 1995; Venier *et al.*, 1994), or tangent correlations (Ott *et al.*, 1993). An alternative approach is to use applied forces, including hydrodynamic flow (Kurz and Williams, 1995; Venier *et al.*, 1994), optical trapping (Felgner *et al.*, 1997, 1996; Kurachi *et al.*, 1995; Takasone *et al.*, 2002), and atomic force microscopy (Kis *et al.*, 2002).

Once EI is known, the deformation of the microtubule can, in principle, be used to estimate the distribution of load on the microtubule. However, to date there has not been, to our knowledge, an estimate of EI *in vivo*. The only information available therefore is the deformation of the microtubule, characterized by the curvature distribution (Odde *et al.*, 1999). It is important to note that EI and the curvature distribution are directly related (discussed below) when the only forces are thermal. However, microtubule bending in living cells is unlikely to be driven solely by thermal forces. The curvature distribution therefore serves, as the principal characterization of microtubule bending, and so the methods used to estimate it will be the focus of this chapter.

There are various ways to estimate local curvature and construct a distribution. One method involves fitting a circle to a specific part of the microtubule to estimate the curvature, since for a given circle the curvature is the reciprocal of the radius (Cassimeris *et al.*, 2001; Gupton *et al.*, 2002; Waterman-Storer and Salmon, 1997). A similar, yet simpler approach is to use three adjacent points along the microtubule's contour to calculate the angle change with respect to the arc length, namely the three-point method (Odde *et al.*, 1999). This method provides a simple estimate of local curvature and does not require knowledge of the microtubule's position or curvature at its ends, that is the boundary conditions. Alternatively, microtubule shapes can be fit to a set of basis functions, such as cosines, sines, and polynomials, and the curvature calculated analytically. In this chapter, we focus on estimating the curvature distribution using both the three-point and the shape-fitting methods.

In order to determine the accuracy of a given method, it is necessary to know the underlying microtubule shape. This presents an immediate problem because the image used for collecting the x - y coordinates of the microtubule is noisy, digitized, and blurred by diffraction from a circular aperture in the microscope. To address this problem, we used a computational model to simulate both the bending of a thermally driven semiflexible polymer, as well as the subsequent digital imaging via fluorescence microscopy, an approach that we call model-convolution microscopy (Sprague *et al.*, 2003). This allows us to construct essentially exact simulated data sets (where the position of the fluorescent object, the deformed microtubule, is known to the computer's decimal accuracy), which can then be used to validate the accuracy of each method in terms of its ability to properly reproduce the (known) curvature distribution. Although the method is general, we will analyze the particular case of thermally driven microtubules as observed *in vitro*. From the insight we gain through the simulations, we are able to determine the pitfalls associated with estimating the curvature distribution from experimental data. Finally, we discuss extending the method to analyze microtubule deformation in living cells.

III. Raw Data Collection

Modern optical microscopes with high numerical aperture (NA) objectives coupled with scientific grade digital cameras are routinely used to gather digital images of microstructure within the cell. Both differential interference-contrast (DIC) microscopy and fluorescence microscopy are commonly used to visualize microtubules, with DIC usually dominating *in vitro* observations and fluorescence microscopy dominating *in vivo* applications. While the details of each type of microscopy ultimately affect the quality of the collected images, both methods provide digital images of microtubules as sources of raw data. An example of an image taken with our microscope of

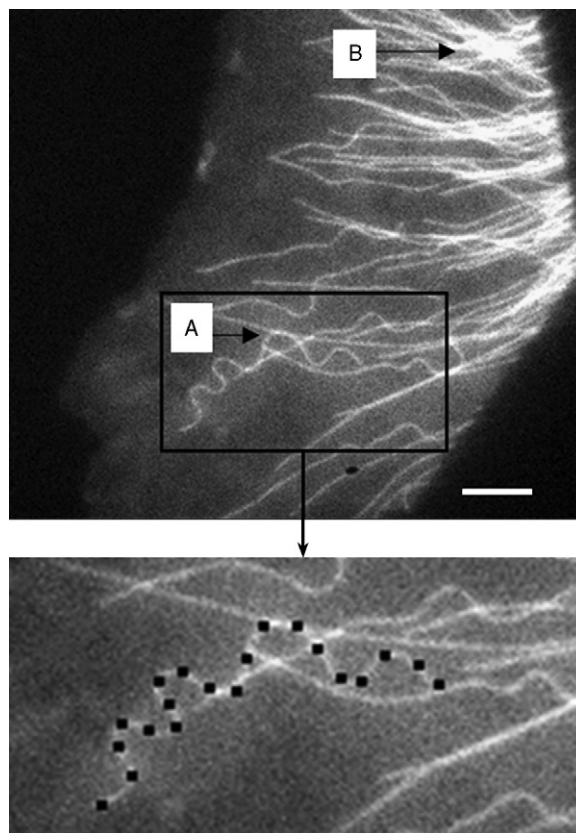


Fig. 1 Typical digital image of EGFP-labeled microtubules taken from the lamella of an epithelial cell. The image was acquired using a $60\times$, 1.4-NA Plan APO oil immersion objective with a $2.5\times$ projection lens. Note that the deformation observed in living cells is highly variable. The arrows indicate regions where crossover (A) and high density (B) of microtubules makes determination of the microtubule shape ambiguous. The inset shows typical x - y coordinates collected from a highly curved microtubule. To remain in focus, the z -coordinates must remain within about $0.5\ \mu\text{m}$ of each other, and so the microtubules that are in focus all along their length can be approximated as deforming in the x - y plane only. Scale bar is $4\ \mu\text{m}$.

fluorescently labeled microtubules in a living epithelial cell stably transfected with GFP-tubulin (Rusan *et al.*, 2001) is shown in Fig. 1.

Once digital images of microtubules have been collected, individual microtubules need to be identified. While this is usually trivial with *in vitro* data, it can be difficult with *in vivo* images because microtubules are rarely visible along their entire length and frequently cross over each other. In addition, the high density of microtubules in some regions of the cell body makes identifying single microtubules very difficult (Fig. 1). To deal with these problems, we collect data from the edges of cells, typically in the lamella of epithelial cells, where individual microtubules can clearly be distinguished. Data is collected from the plus-end of a microtubule back to a point where the position of the microtubule becomes difficult to determine visually. Finally, data is excluded from microtubules that ambiguously cross over each other.

A. Point-Click Method

On defining a microtubule of interest, the x - y coordinates of the microtubule are extracted from the image. Since the depth of field of a 1.4-NA lens is $\sim 0.5 \mu\text{m}$, we assume that if the entire length of a microtubule (~ 10 – $30 \mu\text{m}$) is in focus, its position is essentially limited to a plane (i.e., the focal plane). A simple method to visually extract the positional information is to use image-processing software such as ImageJ (public domain, <http://rsb.info.nih.gov/ij/>) or MetaMorph (Molecular Devices Corporation, Downingtown, Pennsylvania) to view the digital images and record the x - y coordinates that correspond to positions on the microtubule at regular intervals. This is commonly done by hand with a mouse-controlled cursor, by moving the pointing arrow over the position of the microtubule and then clicking the button to record the pixel coordinates. Most image-processing software has a feature to automatically collect this data. For example, in MetaMorph, the “measure pixel” function is set up to record the x - y coordinates from any position in the image by “clicking” on the feature of interest. These data points are then exported to MatLab 7.1 (The Mathworks, Natick, Massachusetts) for later analysis. While this method is simple, it is prone to errors from visually aligning the mouse pointer with the center of the projected image of the microtubule.

B. Semiautomated Methods

Semiautomated image-processing algorithms can make the recording of the coordinates more precise. Janson and Dogterom (2004) presented a semiautomated method for collection of digitized coordinates in a DIC image of an *in vitro* microtubule. Briefly, to maximize contrast, they selected microtubules orthogonal to the direction of greatest optical shear in the DIC microscope. They then obtained line scans perpendicular to the microtubule across every pixel column in a region and convolved the line scans with one period of a sine function which mimics the shadow-cast appearance of DIC images. This one-dimensional sine wave convolution effectively acts as a pattern recognition filter and amplifies the true signal of the

microtubule, which increases the accuracy of the raw data collection process. However, this method is specific to DIC microscopy as it capitalizes on the contrast pattern inherent to DIC microscopy, and would need to be modified for fluorescent images, that is with a Gaussian function or a Bessel's function squared, to mimic the point spread function of light. In principle, such semiautomated methods for collecting positional data from within fluorescently labeled cells could be developed to increase positional accuracy.

C. Data Collection Errors

Accurate collection of raw data is important because the methods described above for extracting positional data effectively discretize the microtubule from a “continuum” into a set of discrete coordinate values. The coordinates are then used to estimate the curvature, and the degree of uncertainty in these coordinates directly affects the associated uncertainty in the estimate. In [Sections III.C.1 and III.C.2](#), we discuss sources of error attributed to collecting coordinates from digital images.

1. Digitization Error

A charge-coupled device (CCD) camera is an array of pixels (picture elements) that detect light and transfer it to a digital array (image). Since each pixel sums the light intensity projected onto it, the resulting image array will lose spatial information with increasing pixel size. This leads to the first type of error associated with collecting data from a digital image, which we will refer to as “digitization error.” For a single image, the digitization of data determines the smallest detectable deformation of the microtubule; according to the Nyquist limit, it is twice the pixel size.

Because the microtubule is only 25 nm in diameter, optical microscopes utilize high-NA lenses, typically 1.30 or higher, to maximize the resolution (typically ~200–250 nm). In addition, high magnification allows for projecting the image onto more pixels, which results in better sampling and less digitization error. However, there is a practical limit to the magnification, due to concerns of signal-to-noise ratio. When the magnification is increased, the intensity of the signal from the image is spread over more pixels and eventually the noise in each pixel starts to mask the signal. Therefore, to achieve high-quality images of fluorescently labeled microtubules, a typical experimental setup might include a 60 \times , 1.4-NA objective with a 2.5 \times projection lens for a resulting camera magnification of 150 \times . The digital image is obtained by a cooled CCD camera which has a physical pixel dimension of $\sim 8\text{ }\mu\text{m}$. In this setup, the resulting pixel dimension in the image, which we will term the image pixel size, is $\sim 50\text{ nm}$. When extracting microtubule coordinates in this setup, the digitization errors from the image pixel size (50 nm) are large compared to the diameter of the microtubule (25 nm). As an example, a perfectly straight microtubule aligned diagonally with respect to the

pixel array will look like a step function when digitized. In this extreme case, the calculated radius of curvature when using every point could be as small as 32 nm.

2. Measurement Error

Another source of error is introduced by the method used to select the x - y coordinates of the microtubule. If an individual coordinate selected from an image deviates from the true position on the microtubule, the resulting estimate of curvature will likely be overestimated. This can be understood by thinking of a straight microtubule. If the selected coordinates for a perfectly straight microtubule do not fall exactly on a line, the curvature of that microtubule will artificially increase, introducing error in data collection. Throughout this chapter, we will call these deviations from the true position of the microtubule “measurement error.” Note that the impact of this error on the curvature estimate will be additive to the errors introduced by digitization (discussed further in [Section IV.B.4](#)).

IV. Validation Strategy

To assess the accuracy of any particular curvature estimation method, it is necessary to have test cases where the actual coordinates of the microtubule contour are known with high precision. In order to establish these test cases, we utilize a computer algorithm to generate a large ensemble of equilibrium semiflexible polymer configurations, which simulate microtubules. Using these simulated polymers allows us to eliminate the problem of experimental error and perform a quantitative comparison of different analysis methods. In addition, we can simulate the spread of light due to diffraction and the uncertainties in estimating the position of the microtubules due to digitization and measurement errors. We then determine how much each of these errors affects the final curvature distribution estimate. Also, since microtubules observed in living cells often appear more curved than microtubules *in vitro*, we vary the shape undulation of simulated microtubules by changing the persistence length, the characteristic distance over which the tangent angles become uncorrelated, over four orders of magnitude. This allows us to test the ability of various methods to estimate the curvature over a wide range of shapes.

For a thermally driven polymer, the average angle spanned by the tangent angles at any two points along the curve $s_1 = 0$ and $s_2 = s$ is given by

$$\langle \vec{t}(s) \cdot \vec{t}(0) \rangle = \langle \cos[\theta(s) - \theta(0)] \rangle = \exp\left(-\frac{s}{2L_p}\right) \quad (1)$$

in two dimensions, where \vec{t} is the tangent vector along a curve parameterized by s ([Fig. 2](#)). Since the choice of origin is arbitrary, we chose, for simplicity, the left end of the microtubule to be the origin ($s_1 = 0$). The characteristic distance at which this average angular span, or “tangent correlation,” decays to $1/\sqrt{e}$ geometrically

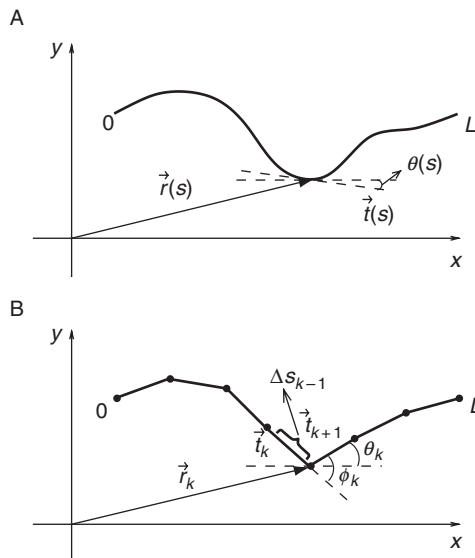


Fig. 2 Continuum versus discrete representations of a polymer. (A) A polymer of length L is described by the curve $\vec{r}(s)$ in the x - y plane, where s denotes the position along the contour. The variables $\vec{r}(s)$ and $\theta(s)$ are the tangent vector and the angle it makes with the horizontal axis at a point s , respectively. (B) The continuum curve in (A) is discretized. The tangent vector and the angle with the x -axis are now defined at coordinates $\vec{r}_k = (x_k, y_k)$. The variable ϕ_k denotes the angle between consecutive tangent vectors \vec{r}_k and \vec{r}_{k+1} , and Δs_k is the spacing between neighboring coordinates \vec{r}_k and \vec{r}_{k+1} .

defines the persistence length, L_p . In the case where curvature is driven by thermal forces alone, equipartition of energy can be used to show that L_p is related to the temperature, T , and flexural rigidity by (Howard, 2001)

$$L_p = \frac{EI}{k_B T} \quad (2)$$

where k_B is Boltzmann's constant.

In three dimensions, the tangent correlations decay twice as quickly as that shown in Eq. (1), due to an additional angular degree of freedom (Howard, 2001). Note that Eq. (1) is not universal, but rather depends on the polymer model used as well as the forces acting on the system. For example, it was shown that tangent correlations exhibit oscillatory decay for polymer models with a nonzero diameter (Marenduzzo *et al.*, 2005). One might speculate that for systems with additional nonthermal forces, the tangent correlations will have nonexponential decay. For example: (1) extensional forces suppress fluctuations and compressional forces tend to introduce buckles (Fygenson *et al.*, 1997) and (2) lateral confinement forces tend to suppress fluctuations (Brangwynne *et al.*, 2006).

A. Modeling of Semiflexible Polymers

Our approach is to model the microtubule as a discrete chain embedded in a solvent, which may be described using a stochastic model for fluid flow ([Ihle and Kroll, 2001](#); [Malevanets and Kapral, 1999, 2000](#)), often referred to as stochastic rotation dynamics (SRD). SRD is an attractive simulation tool for the coarse-grained modeling of a fluctuating solvent, in particular colloidal and polymer suspensions, since it provides the correct hydrodynamic interactions between embedded particles and fully incorporates thermal fluctuations. For details regarding the algorithm and its transport properties, the reader is referred to a series of articles ([Ihle and Kroll, 2003a,b](#); [Ihle et al., 2004, 2005](#); [Tüzel et al., 2003, 2006](#)).

In the continuum approach, the conformation of a semiflexible polymer such as a single microtubule can be described by a curve $\vec{r}(s)$, where s is the contour position along the curve ([Fig. 2A](#)). Semiflexible polymers are often assumed to be inextensible so that the only relevant potential energy is the bending energy, given by

$$U_b = \frac{1}{2}EI \int_0^L \kappa^2 ds = \frac{1}{2}EI \int_0^L \left(\frac{d\vec{t}(s)}{ds} \right)^2 ds = \frac{1}{2}EI \int_0^L \left| \frac{d\theta(s)}{ds} \right|^2 ds \quad (3)$$

where $\kappa \equiv |d\theta(s)/ds|$ is the curvature, L is the total length of the polymer, $\vec{t}(s)$ is the unit tangent vector at a point s , and $\theta(s)$ is the angle of the tangent vector relative to the x -axis ([Fig. 2A](#)). The correct discretization for the bending energy in [Eq. \(3\)](#) is ([Klapper and Qian, 1998](#))

$$U_b = \frac{1}{2}EI \sum_{k=1}^{N-1} \frac{(\vec{t}_{k+1} - \vec{t}_k)^2}{(\vec{r}_{k+1} - \vec{r}_k)^2} \cdot \Delta s_k \quad (4)$$

where N is the total number of nodes (x - y coordinate pairs) on the discrete chain in the simulation. Here the magnitude of the distance between two consecutive coordinate pairs in a chain is given by $\Delta s_k \equiv |\vec{r}_{k+1} - \vec{r}_k|$. [Figure 2B](#) shows the discretized position and tangent vectors. Coupling to the solvent is described by including the polymer nodes in the SRD collision step (see [Malevanets and Yeomans, 2000](#) for details).

The time evolution of the polymer between collisions is determined by solving the resulting Newton's equations of motion using the velocity Verlet algorithm ([Frenkel and Smit, 2002](#)). We will refer to this procedure as a hybrid SRD-MD simulation. A typical snapshot of a single semiflexible polymer in solvent is shown in [Fig. 3](#). This approach has been used previously to study the behavior of polymers in solution. In particular, [Malevanets and Yeomans \(2000\)](#) studied the dynamics of short polymer chains and [Kikuchi et al. \(2002\)](#) investigated polymer collapse in the presence of hydrodynamic interactions using this approach. SRD has been used to investigate the effects of hydrodynamic interactions ([Falck et al., 2003](#); [Ripoll et al., 2004](#); [Winkler et al., 2004](#)) on the behavior of rod-like colloids

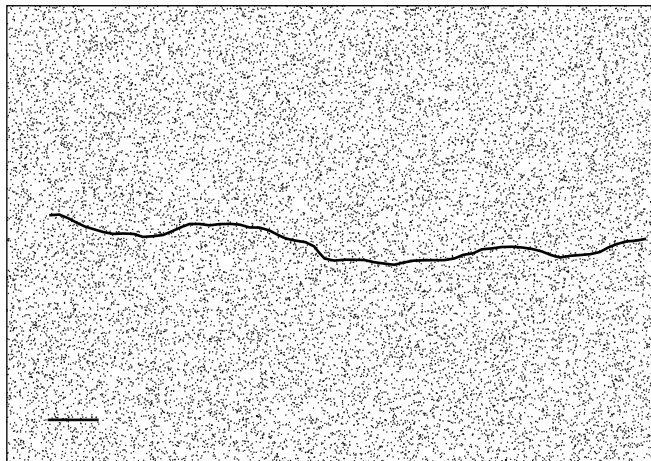


Fig. 3 A snapshot from a hybrid SRD-MD simulation showing a single polymer chain surrounded by solvent particles. Total number of solvent particles is 4.6×10^4 , and the simulation box size is 96×96 pixels. For clarity, a short chain of 64 nodes is shown, the scale bar is 5 pixels and $L/L_p = 6.3$.

and flexible polymer chains in solution. Others have also used SRD as a tool to study colloids ([Falck *et al.*, 2004](#); [Hecht *et al.*, 2005](#); [Padding and Louis, 2004](#)) and vesicles in shear flow ([Noguchi and Gompper, 2004](#)). In this study, SRD provides a heat bath for the polymers.

B. Generation of Simulated Data

Using hybrid SRD-MD, we simulated the bending of thermally driven polymers to test each shape parameterization method. Since microtubules in a cell appear to bend much more than their counterparts from *in vitro* experiments, we are unsure if the persistence length (L_p) for microtubules in a cell is the same as the L_p estimated from *in vitro* experiments. If the persistence lengths are different, then either the EI is different or additional forces are acting on the microtubules within the cell that increase the apparent flexibility. To examine this effect, we simulated polymers with a wide range of persistence lengths, L_p . In particular, we studied polymers of length L for which $0.03 \leq L/L_p \leq 62$. This range of persistence lengths allowed us to test the shape parameterization methods across a wide range of flexibility regimes in an attempt to find a robust method for curvature distribution estimation that works for all persistence lengths, or at least to determine where each method breaks down ([Fig. 4](#)). Note that when L/L_p is much smaller than one, the filament is essentially straight, and when L/L_p is larger than one, the filament is highly flexible. For most biologically relevant polymers, L/L_p is of order 1, and is described properly using semiflexible chain models ([Storm *et al.*, 2005](#)).

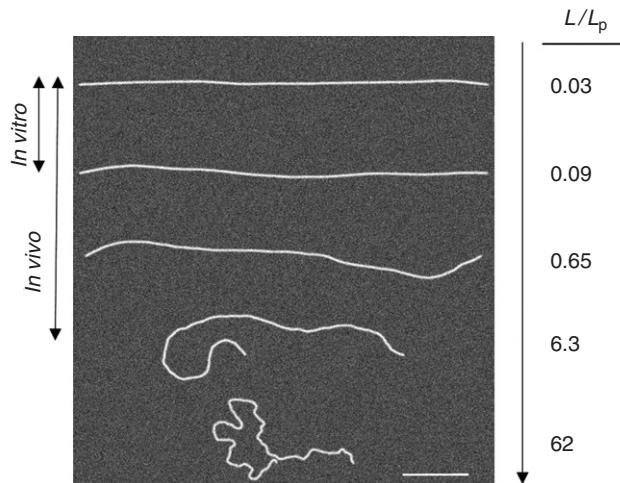


Fig. 4 Representative examples of simulated thermally driven polymers having $L/L_p = 0.03, 0.09, 0.65, 6.3, 62$ from top to bottom, respectively. Each chain has been convolved with the point spread function and Gaussian white noise to create a simulated fluorescent image of the polymer. We observe microtubules within the cell with shapes similar to the first four images. Scale bar is $5 \mu\text{m}$.

1. Simulation Conversion Factor

We simulated $M = 500$ thermally driven polymers for different values of L/L_p , with representative examples shown in Fig. 4. To convert between physical length and the dimensionless simulation units, we set the bond length (distance between consecutive coordinates) in the polymer chain to be equal to 1 pixel. The reason for this is twofold. First, the pixel is a pseudo-dimensionless unit that can be directly compared to any experimental setup. Second, the pixel is the smallest unit of resolution in the experimental data. Therefore, it is a natural choice for the conversion factor. The polymers in our simulations consist of 622 nodes which correspond to a length of 621 pixels. If we take 50 nm as a pixel size, an approximate value for a typical high-resolution microscopy system, then our polymer length is $\sim 31 \mu\text{m}$. This length is typical for *in vitro* measurements of microtubule shapes (Gittes *et al.*, 1993; Janson and Dogterom, 2004), and the simulated polymers can always be truncated to a shorter length that might more closely match the length of microtubules observed *in vivo*.

2. Model Convolution Microscopy

The position of each coordinate in the hybrid SRD-MD simulations is accurate to decimal precision of 1×10^{-7} so that the simulated data can be thought of as pure and devoid of any measurement error. This pure data provides the best-case

scenario for each shape parameterization method used to estimate the curvature distribution. However, in any experimental system, such as the one described in [Section III.C.1](#), the digital image is always contaminated with noise from the detector and optical aberration from the microscope. In addition, the spread of light due to a circular aperture blurs the image and makes the microtubules appear much wider than they actually are. When taken together, these sources of noise and blur make accurate collection of x - y coordinates difficult. To simulate noise and blur, we convolved our pure data with the characteristics of the microscope system to approximate experimental data, a method called model convolution microscopy ([Sprague *et al.*, 2003](#)). Our procedure was as follows:

- a. We took 35 independent simulations of polymers with $L/L_p \cong 0.02$ and projected the pure data onto a 5-nm two-dimensional grid.
- b. The grid was filled in to make the simulated chains appear 25-nm wide, corresponding to the width of a microtubule.
- c. The projected polymer data was convolved with the point spread function, effectively making every location within the polymer a point source of light.
- d. The signal and background levels were normalized to experimentally measured levels typical for EGFP-labeled microtubules imaged from LLC-PK1- α epithelial cells.
- e. The fine grid was coarse grained to a larger grid size of 50 nm, approximately corresponding to the size of pixels in our microscope system.
- f. The noise due to collecting the image with a digital camera was estimated by calculating the variance of the intensity for a typical background region in an experimental image, and by adding Gaussian white noise with a similar variance.

This procedure resulted in an image of a simulated polymer that is directly comparable to an image collected experimentally from a fluorescently labeled microtubule *in vivo* with two important exceptions: (1) we know the precise position of the underlying polymer and (2) we know its persistence length ([Fig. 4](#)).

3. Estimation of Digitization Error

Whenever data are binned (i.e., pixelated), there is loss of information. Therefore, digitization errors are inherent in all digital images. Since we set the units for our pure coordinate pairs in the simulation to be equivalent to pixels in a digital image, the correct digitization is achieved by simply rounding the pure coordinate values to integer values corresponding to the nearest pixel location. This is analogous to the binning action that a CCD camera performs on every pixel in an experimental image.

4. Estimation of Measurement Error

We used very stiff simulated polymers ($L/L_p = 0.02$) and rotated them so that their end points were both on the x -axis. We applied model convolution microscopy to the polymers and obtained simulated images. In practice these simulated images appeared very straight, and it was therefore reasonable to assume that the measurement errors from point clicking were limited to deviations in the y -direction only.

We first collected x - y coordinates from simulated images using the point-click method. We then overlaid the estimated pixel locations onto the digitized microtubule image to determine the magnitude of the deviations in pixel units in the transverse (y) direction only, which are an estimate of our measurement error. The distribution of a one-dimensional measurement error is shown in Fig. 5 in units of pixels, with one pixel corresponding to 50 nm for the experimental system described in III.C.1. The histogram indicates an error (standard deviation) of 52 nm. (Note that for any other pixel size, another corresponding histogram needs to be constructed.)

The measurement of a highly curved microtubule is expected to have deviations in the x -direction as well as the y -direction. So, one can use the one-dimensional error as a lookup table independent of direction by assuming the deviations in x and y are statistically independent and equal. Therefore, the root-mean-squared (RMS) magnitude of a two-dimensional measurement error is ~ 74 nm. When compared to an earlier estimation of measurement error by Gildersleeve *et al.* (1992)

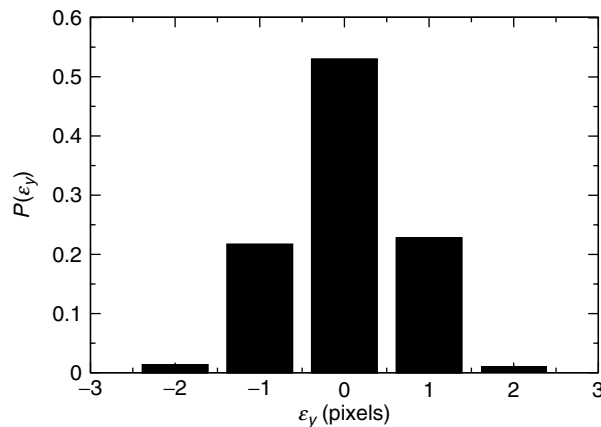


Fig. 5 Histogram of the magnitude of measurement errors in y -direction, namely ϵ_y , calculated using data collected from 35 simulated polymers. The RMS error is 52 nm and 97% of the time the clicking error is 0 or 1 pixels. The total number of data points used to construct the histogram is 1463. Note that one pixel corresponds to 50 nm in the experimental system, and therefore, for any other image pixel size, the histogram needs to be reconstructed.

(RMS deviation of 162 nm), our system is roughly twice as accurate (note: Gildersleeve *et al.* were tracking microtubule tips using DIC, which is more difficult than tracking the position of the microtubule using fluorescence). Since the values in the lookup table have units of pixels, they can be directly added to the simulated polymer coordinates. Therefore, to recreate the measurement error associated with the point-click method in our simulated polymers, we randomly picked two values from the measurement error lookup table and added each value to the x and y coordinates, respectively.

5. Coarse-Graining

Since each position estimate contains errors as described above, the coordinate data from a microtubule must be collected at some larger interval to reduce the effects of measurement error on the estimation of curvature. For example, if the point-click method is used to collect the coordinates from every adjacent pixel, the magnitude of the measurement error will dominate and will result in a noisy estimate of the x - y coordinates. Further, if this data is then used to estimate a curvature distribution, the effect of the measurement noise will substantially alter the associated curvature distribution toward that of a more flexible polymer. Therefore, when the RMS measurement error approaches the size of a pixel, the x - y coordinates should be sampled at some lower spatial frequency to reduce the effects of measurement error, a practice we use for coarse-graining. At the other extreme, if the data is collected at too low a spatial frequency, sharp fluctuations in the microtubule's shape between sampling points will be missed, and the resulting curvature estimate will underestimate the bending. Therefore, some optimum must exist between these two extremes that provides the most accurate estimate of the curvature distribution.

In order to investigate the effect of coarse-graining, we skipped coordinates in the simulated images, effectively increasing the distance between nodes. We use the resulting average spacing, $\Delta\tilde{s}$, as a measure of the coarse-graining. Because the uncertainty in our collected coordinates is a maximum of 2 pixels in any direction, and since we do not want overlapping data points, the minimum spacing between coordinates for data collected by the point-click method should be at least 5 pixels. In the experimental system described by [Odde *et al.* \(1999\)](#), their coordinate spacing was $\sim 0.5\ \mu\text{m}$, which corresponds to a spacing of $\Delta\tilde{s} = 10$ pixels. Note that $\Delta\tilde{s}$ should always be smaller than the persistence length, since using spacing larger than the persistence length will miss the correlations in the polymer shape along the length and result in significant entropic contributions to the polymer conformation ([De Gennes, 1979](#); [Doi and Edwards, 2004](#)).

Applying the processes described above to the simulation data results in three sets of simulated data: pure, digitized, and digitized with measurement error. [Figure 6](#) shows all three sets of data from representative simulated polymers at two different values for L/L_p . Note for a stiff polymer, $L/L_p = 0.03$ ([Fig. 6A](#)), the

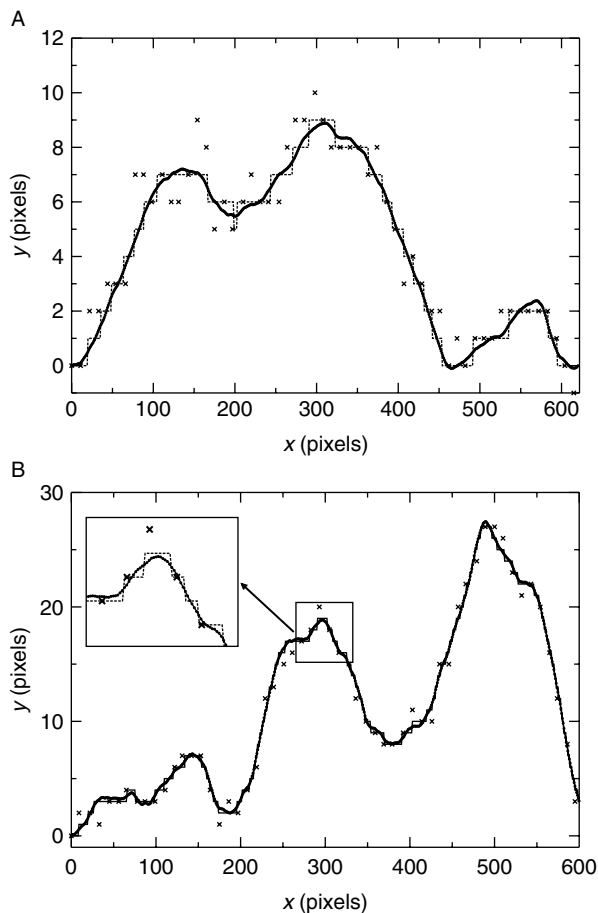


Fig. 6 Simulated polymer chains after digitization and the addition of measurement errors. Bullets show pure data, dashed lines show the effect of digitization, and crosses show the data after digitization and measurement error addition. (A) $L/L_p = 0.03$ and (B) $L/L_p = 0.65$. The inset in (B) shows a close-up of a highly curved region.

relative effects of the digitization and measurement errors are larger than for a more flexible polymer, $L/L_p = 0.65$ (Fig. 6B).

C. Validation of Semiflexible Polymer Simulation

The hybrid SRD-MD simulations correctly reproduce the statistics of thermally driven polymers. We measured tangent correlations (Ott *et al.*, 1993) and end-to-end fluctuations (Van Noort *et al.*, 2003), and found that the results all agree with

analytical predictions of polymer theory (not shown). However, we also wanted to validate the simulation's ability to correctly incorporate noise and reproduce experimental data. Our strategy to ensure that the model and noise simulation were working properly was to apply a bending mode analysis to our simulated data to determine whether we could recreate the results of [Gittes *et al.* \(1993\)](#) and [Howard \(2001\)](#).

A bending mode analysis can be used to measure the flexural rigidity of *in vitro* microtubules by expressing the polymer's shape as a superposition of a large number of Fourier cosine modes ([Gittes *et al.*, 1993](#)). Using a Fourier series expansion, the shape $\theta(s)$ of a microtubule can be expressed by

$$\theta(s) = \sqrt{\frac{2}{L}} \sum_{n=0}^{\infty} a_n \cos\left(\frac{n\pi s}{L}\right) \quad (5)$$

where a_n denotes the amplitude of the n th cosine mode. For a discrete chain, s will be replaced by s_k^{mid} and the sum is limited to $N - 1$. The spacing between coordinates is given by

$$\Delta s_k = \sqrt{(x_{k+1} - x_k)^2 + (y_{k+1} - y_k)^2} \quad (6)$$

which yields for the position along the contour

$$s_k^{\text{mid}} = \frac{1}{2} \Delta s_k + \sum_{i=1}^{k-1} \Delta s_i \quad (7)$$

Using the orthogonality of cosine functions, one can show that

$$a_n = \sqrt{\frac{2}{L}} \int_0^L \theta(s) \cos\left(\frac{n\pi s}{L}\right) ds \cong \sqrt{\frac{2}{L}} \sum_{k=1}^N \theta_k \Delta s_k \cos\left(\frac{n\pi s_k^{\text{mid}}}{L}\right) \quad (8)$$

Here the tangent angle is given by

$$\theta_k = \tan^{-1} \left(\frac{y_{k+1} - y_k}{x_{k+1} - x_k} \right) \quad (9)$$

The discrete coordinates from the polymers are used to solve for the mode amplitudes using [Eq. \(8\)](#), and the variance of mode amplitudes $\text{var}(a_n)$ computed from all polymers is used to estimate the flexural rigidity. In theory, each cosine mode yields an independent measure of flexural rigidity. For a more detailed description of the method see [Gittes *et al.* \(1993\)](#).

We computed the mode amplitudes for 500 simulated polymers and calculated the variance. Using equipartition of energy, the variance of the mode amplitudes can be expressed as

$$\text{var}(a_n) = \langle a_n^2 \rangle = \frac{k_B T}{EI} \left(\frac{L}{n\pi} \right)^2 \quad (10)$$

Note that the mean of the mode amplitudes is equal to zero since the simulated polymers have no intrinsic curvature. As can be seen from Eq. (10), the variance for each mode should scale as $1/n^2$ where n is the mode number. Plotting the variance of mode amplitudes against the mode number (Fig. 7A) shows good agreement with theory.

Next, we simulated the effects of digitization and measurement error as discussed in Sections IV.B.3 and IV.B.4, respectively. In addition, the data was

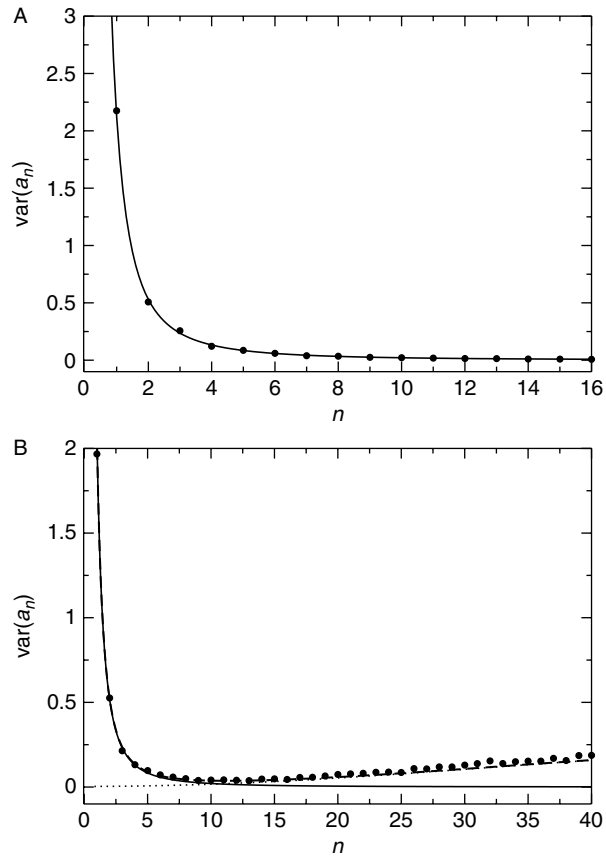


Fig. 7 Validation of hybrid SRD-MD simulation. Variance of the mode amplitude a_n as a function of the mode number n is shown in bullets (A) for the pure simulation data and (B) for the digitized data with measurement error. Solid line is a plot of Eq. (10). Dotted and dashed lines represent theoretical predictions given by Eqs. (11) and (12), respectively. The results match well the relationship for experimental data presented by Gittes *et al.* (1993).

coarse-grained at an interval of $\Delta\tilde{s} = 10$ pixels. To compare our simulated noisy data to theory, we used the relation

$$\langle a_n^2 \rangle^{\text{noise}} = \frac{4}{L} \langle \varepsilon_y^2 \rangle \left[1 + (N-1) \sin^2 \left(\frac{n\pi}{2N} \right) \right] \quad (11)$$

for the variance of noise reported by [Gittes *et al.* \(1993\)](#). Here ε_y is the magnitude of the measurement error in pixels, from our measurement error lookup table ([Fig. 5](#)). The noise variance can be directly added to the theoretical mode variance, which yields

$$\text{var}(a_n)^{\text{measured}} = \frac{1}{L_p} \left(\frac{L}{n\pi} \right)^2 + \frac{4}{L} \langle \varepsilon_y^2 \rangle \left[1 + (N-1) \sin^2 \left(\frac{n\pi}{2N} \right) \right] \quad (12)$$

for the measured variance. We plotted the measured variance, calculated using the digitized data with measurement error, against the mode number and the results are shown in [Fig. 7B](#). The agreement with [Eq. \(12\)](#) is excellent indicating that we are able to correctly reproduce the experimental results of [Gittes *et al.* \(1993\)](#) using the hybrid SRD-MD simulations. In [Section V](#), we discuss methods to estimate the curvature distribution.

V. Curvature Estimation Methods

A. Three-Point Method

A simple method was used by [Odde *et al.* \(1999\)](#) to determine the curvature at which microtubules broke, as well as the curvature distribution of all microtubules in the lamella of fibroblasts. They collected x - y coordinate data from fluorescent images every 500 nm along the length of microtubules in Swiss 3T3 fibroblasts. The curvature (κ) was calculated at each coordinate by taking three adjacent points and computing the change in the angle (ϕ_k) ([Fig. 2](#)) over the average arc length of the two adjacent segments to yield

$$\kappa \approx \left| \frac{2\phi_k}{\Delta s_{k-1} + \Delta s_k} \right| \quad (13)$$

which is an approximation of the curvature for small angle changes and small bond lengths.

B. Shape-Fitting Method

We thought it natural to extend the bending mode analysis ([Gittes *et al.*, 1993](#)) to estimate the curvature distribution. Our strategy is again to map the shape, $\theta(s)$ of the microtubule to a sum of cosine waves, and calculate curvature at the nodes along the microtubule's length and then produce the curvature distribution. Differentiating [Eq. \(5\)](#) with respect to s , we have

$$\kappa = \left| \frac{d\theta(s)}{ds} \right| = \left| \sqrt{\frac{2}{L}} \sum_{n=0}^{\infty} a_n \left(\frac{n\pi}{L} \right) \sin \left(\frac{n\pi s}{L} \right) \right| \quad (14)$$

for the curvature. Note that Eqs. (5) and (14) are given in terms of the contour length, s , and in the discrete approximation, s is replaced by s_k^{mid} as shown in Eq. (7).

Alternatively, one can use other analytical functions to map the shape of a microtubule. For example, sine and cosine transforms or polynomials can be fit to the shape and used to estimate $\theta(s)$ or the curvature $d\theta(s)/ds$. While the selection of the analytical function seems arbitrary, a complete set of basis functions ([Arfken and Weber, 2001](#)) is needed to correctly reconstruct the microtubule's shape.

C. Constructing the Curvature Distribution

The curvature distribution can be estimated by creating a histogram of the discrete curvature values obtained from either the three-point method or the shape-fitting method. It is important to note that the number of bins used in the histogram should not exceed the number of discrete values that curvature can take. For stiff microtubules ($L/L_p < 0.65$) and digitized data collected for every pixel this may be as low as three bins.

To determine the accuracy of the curvature distribution, it should be compared to theory. For the case of a thermally driven polymer, the local energy should be distributed exponentially according to Boltzmann's law. Since energy is proportional to the curvature squared, the curvature distribution should be normally distributed, and for polymers with zero mean curvature and unit bond length, will be given by

$$P(\kappa) = \sqrt{\frac{2L_p}{\pi}} e^{(-L_p\kappa^2)/2} \quad (15)$$

The extra factor of $\sqrt{2}$ in the prefactor is because of the curvature distribution being a half Gaussian, which is due in turn to the absolute value in Eq. (5). This equation shows that the variance of the normal distribution of κ equals the reciprocal of persistence length, L_p . The cumulative distribution function, $C(\kappa)$, can be derived from Eq. (15) using the following relation

$$C(\kappa) = \int_0^\kappa P(\kappa') d\kappa' \quad (16)$$

Using Eqs. (15) and (16) it can be shown that

$$C(\kappa) = \text{erf} \left(\sqrt{\frac{L_p}{2}} \kappa \right) \quad (17)$$

where erf is the error function.

The empirical cumulative distribution function is easily generated from the experimental data and it can be compared to Eq. (17). First, begin by sorting all

the discrete curvature values from lowest to highest. The position of each data point in the sorted list is indicated by its index from 0 to $K-1$ where $K = M \cdot N$ is the total number of data points. These curvature values define the x -position for each data point in the distribution. Next, the index for each sorted data point is rescaled between 0 and 1. This effectively performs the integration in Eq. (16), and the y -data is generated. Finally, by plotting the normalized index as a function of the curvature values, the empirical cumulative distribution is generated (Press *et al.*, 1992).

VI. Results

A. Three-Point Method

1. Pure Data

For the case of pure data, the three-point method for calculating curvature accurately reproduced the curvature distribution for the entire range of L/L_p investigated. Typical results are shown in Fig. 8, where it can be seen that the data are in good agreement with the predictions of Eqs. (15) and (17).

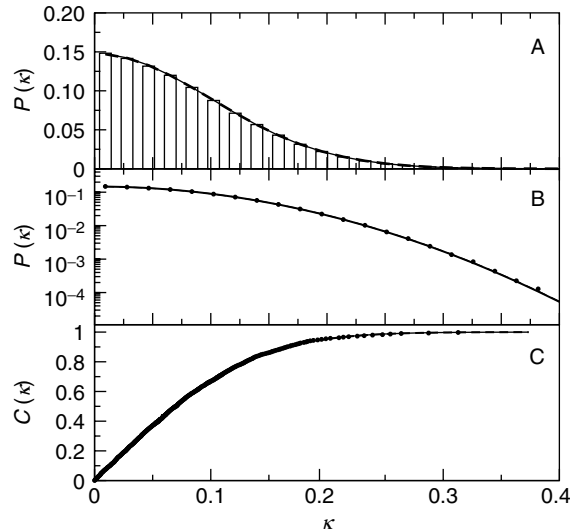


Fig. 8 The estimated probability density (curvature distribution) and cumulative distribution functions for $L/L_p = 6.3$ calculated using pure data. (A) A histogram of the curvature values, κ . (B) Semilog plot of the curvature distribution. The profile is parabolic as expected from a Gaussian distribution. (C) Empirical cumulative distribution function calculated using the sorted curvature data. Solid lines in (A) and (B) show theoretical predictions of Eq. (15), and solid line in (C) shows the theoretical cumulative distribution given by Eq. (17). Dashed lines show the fitted distributions.

We also investigated coarse-graining the data, which is similar to what might be done in a typical experiment with “point-clicked” data. In this case, we found that the variance of the curvature distribution depends on the coarse-graining level. The estimated curvature distribution from simulated polymers with $L/L_p = 6.3$ using $\Delta\tilde{s} = 2$ pixels is shown in Fig. 9. The solid lines in Fig. 9A and B show predictions of Eq. (15), while the solid line in Fig. 9C shows Eq. (17). Comparison with theory shows that the curvature distribution overestimates the small curvatures and underestimates the large curvatures. This is due to smoothing the sharp curvature fluctuations when coarse-graining. Note that Eq. (15) is derived under the assumption that the *local* energy (i.e., energy per unit length) is Boltzmann distributed, and since the total energy of a polymer chain is constant, the local energy must be rescaled on coarse-graining. The rescaling of the local energy can be represented by an effective persistence length, \tilde{L}_p . This can be understood in the following way. Let us start with a polymer chain of N nodes and total length L . Coarse-graining the polymer chain by taking every other coordinate results in a chain of $N/2$ nodes with twice the distance between coordinates. If the spacing between the coordinates in the coarse-grained chain is scaled back to the original node spacing, then the total length will be reduced by a factor of 2. This means the ratio L/L_p is reduced by the same factor, which is equivalent to having an effective persistence length twice the value of L_p . This scaling argument is intended for illustration; in

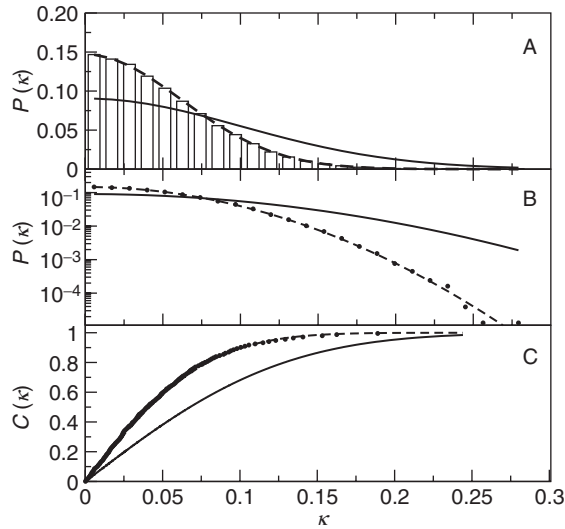


Fig. 9 The estimated probability density (curvature distribution) and cumulative distribution functions for $L/L_p = 6.3$ for a coarse-graining level of $\Delta\tilde{s} = 2$ pixels, calculated using pure data. (A) A histogram of the curvature values, κ . (B) Semilog plot of the curvature distribution. (C) Empirical cumulative distribution function calculated using the sorted curvature data. Solid lines in (A) and (B) show theoretical predictions of Eq. (15) using the correct persistence length L_p , and solid line in (C) shows theoretical cumulative distribution given by Eq. (17). Dashed lines show the fitted distributions.

practice, there might be additional dependencies on parameters besides node spacing and a discussion of these is beyond the scope of this chapter.

We found that the effective persistence length scales linearly with the average spacing of coarse-graining, $\Delta\tilde{s}$. The bullets in Fig. 10 show the effective persistence

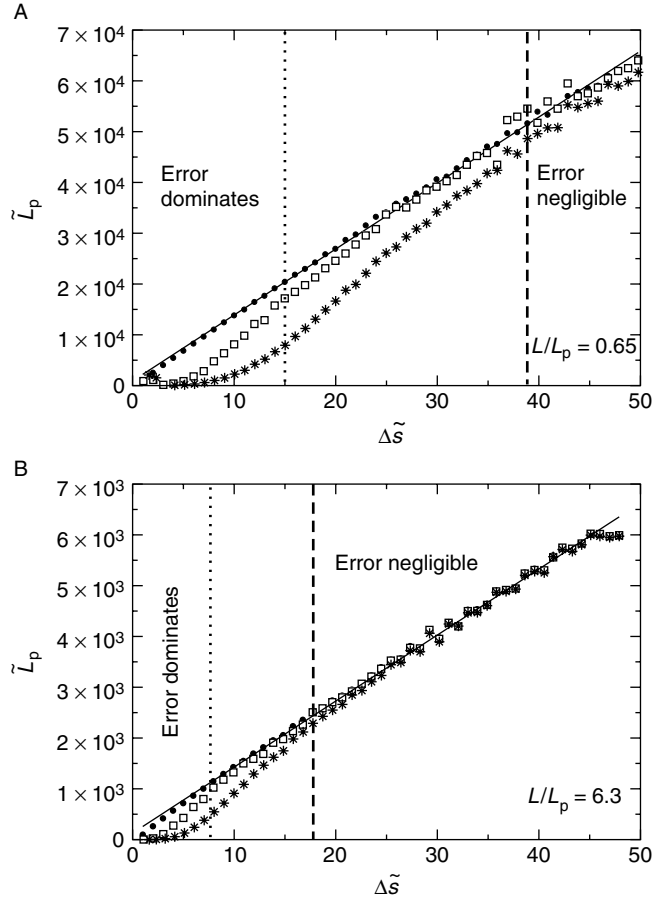


Fig. 10 The effective persistence length \tilde{L}_p as a function of coarse-grained spacing $\Delta\tilde{s}$. The scaling relation is shown for (A) $L/L_p = 0.65$ and (B) $L/L_p = 6.3$, with $L = 621$ pixels. The bullets, empty squares, and stars show results for pure, digitized, and digitized with measurement error data, respectively. The solid line is a fit to the scaling relation for pure data which is used to estimate \tilde{L}_p for a given $\Delta\tilde{s}$. The region to the left of the dotted line corresponds to an error dominated regime (for digitized data with measurement error) where one is mainly measuring the noise contribution to the curvature. The region to the right of the vertical dashed line corresponds to a regime where the noise contribution to the curvature is negligible, and the minimum coarse-graining interval, in principle, is given by this dashed line. However, in practice a value for $\Delta\tilde{s}$ may need to be chosen between the two vertical lines, which will result in some impact of noise on the curvature distribution.

length, \tilde{L}_p , as a function of $\Delta\tilde{s}$, for $L/L_p = 0.65$ and 6.3 . The slope and intercept of the line fitted to the pure data in the figure could be used to estimate the effective persistence length for a given coarse-graining level, $\Delta\tilde{s}$. If this estimated \tilde{L}_p is substituted for L_p in Eq. (15), the resulting curvature distribution is in excellent agreement with the simulation data.

2. Digitized Data

For the case of digitized data, the three-point method had trouble estimating the correct curvature distribution when every data point was used. This is because for a given stiff polymer, that is $L/L_p = 0.03$, the coordinate change from one pixel to the next is small (typically 0 or 1), and the resulting pixel is either directly next to the last pixel or perhaps one pixel above or below. Thus, for digitized data, the resulting calculated curvature values using the three-point method are only one of three values. Furthermore, when the curvature distribution is constructed from this data, the resulting histogram has only three bins, which leads to an imprecise estimate of the curvature distribution.

Alternatively, a more precise estimate of the position could be used, such as a semiautomated method described in Section III.B, to increase the precision of data from integer values of pixel coordinates, to interpolated decimal values corresponding to a position with subpixel precision. With this high precision data, the distribution of angles would not be limited to a few values even if coordinate data was collected from every pixel.

Therefore, to apply the three-point method correctly to digitized data, the coordinates should be coarse-grained, effectively increasing the number of values curvature can take. This means that, just as in the case for pure data described above, the effect of coarse-graining will change the variance of the curvature distribution. The squares in Fig. 10 show the effective persistence length, \tilde{L}_p as a function of $\Delta\tilde{s}$, for $L/L_p = 0.65$ and 6.3 . Whereas the scaling of \tilde{L}_p for pure data was completely linear (bullets in Fig. 10), the plot for digitized data has a nonlinear region for small $\Delta\tilde{s}$ before crossing over to a linear scaling regime at larger spacing. This nonlinear region corresponds to an error dominated regime, and the width varies for each value of L/L_p thereby giving us the minimum coarse-graining interval (coordinate spacing). Note that this procedure provides a quantitative basis to the minimum coarse-graining estimate discussed in Section IV.B.5.

In practice, the observed images of microtubules may not be long enough to sample at large coarse-graining intervals. Therefore, microtubules can be concatenated, as long as the angles at the microtubule ends are matched with each other. This can be accomplished by taking the last two coordinates of one microtubule and aligning them with the first two coordinates of another, with the cost of losing two coordinates (where they overlap) per microtubule.

3. Digitized Data with Measurement Error

Finally, since the data collected from a digital image is also usually biased with measurement error, the real test for the three-point method was to see if it can simultaneously handle both sources of error. Once again the method has trouble when analyzing every pixel of data, but this now has more to do with the magnitude of the measurement error applied to every pixel. This suggests that data should not be collected for every pixel, but rather at some larger interval, similar to the digitized case. The stars in Fig. 10 show the effective persistence length, \tilde{L}_p as a function of $\Delta\tilde{s}$, for $L/L_p = 0.65$ and 6.3. Again the minimum spacing can be determined, and an effective persistence length can be estimated for a given spacing.

The three-point method works well for highly curved polymers as typically observed from *in vivo* microtubule data; however, the method has trouble estimating the curvature of very stiff polymers for $L/L_p = 0.65$ due to noise. To correctly use the method in this stiff regime, the coordinates must be collected more precisely, and/or the data must be coarse-grained to reduce the effect of digitization and measurement error.

The shape of a thermally driven equilibrium polymer with $L/L_p = 6.3$ (Fig. 4) might resemble a highly curved *in vivo* microtubule (shown in Fig. 1 inset). To test how the three-point method performs on polymers with this persistence length, we collected data using the point-click method at a spacing of $\Delta\tilde{s} = 20$, and the resulting curvature distribution is shown in Fig. 11. The solid line shows the agreement of simulation data with Eq. (15) when using the effective persistence length, \tilde{L}_p . Note that the variance of the curvature distribution in Fig. 11 is different from the variance in Fig. 8. A precise knowledge of L_p is needed to rescale the curvature distribution in Fig. 11 and to match the variance in Fig. 8. While the fitted line in Fig. 10 can be used to estimate L_p by extrapolating the line to $\Delta\tilde{s} = 1$, we urge caution in applying this technique to experimental data, as small errors in the slope may lead to large discrepancies in the estimation of L_p . If one chooses to rescale the data to obtain the curvature distribution with the correct variance, a more accurate method for estimating L_p should be used, that is a bending mode analysis.

B. Shape-Fitting Method

We found that the Fourier shape-fitting method can only be applied to estimate the curvature distribution if the correct number of modes is utilized. However, the correct number of modes to use is different for each value of L/L_p , amount of noise, and coarse-graining level investigated. In addition, using the maximum number of modes ($N - 1$) does not necessarily give the correct curvature distribution, as one might expect. This is due to the fact that the sine function in Eq. (13) gives zero curvature values when it is evaluated at the nodes for certain mode numbers.

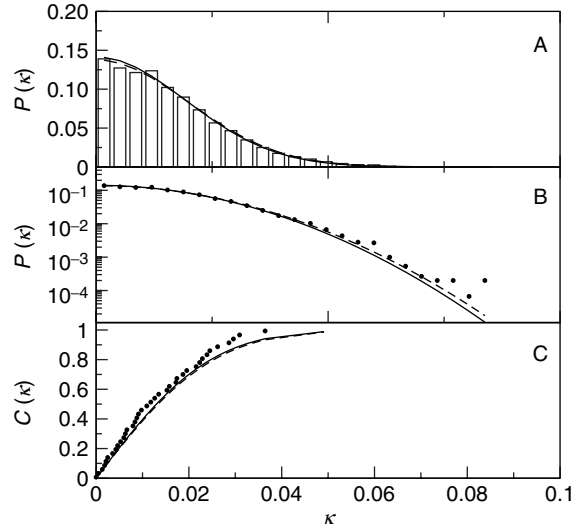


Fig. 11 The estimated probability density (curvature distribution) and cumulative distribution functions for $L/L_p = 6.3$ for a coarse-graining level of $\Delta\tilde{s} = 20$ pixels, for digitized data with measurement error. (A) A histogram of the curvature values, κ . (B) Semilog plot of the curvature distribution. (C) Empirical cumulative distribution function calculated using the sorted curvature data. Solid lines show theoretical predictions of Eqs. (15) and (17), whereas dashed lines show the fitted distribution. Using the effective persistence length, \tilde{L}_p , in Eqs. (15) and (16) rescales the theoretical predictions to match the simulation data.

This happens with increasing frequency for the higher modes, and effectively adds zeros to the curvature distribution, resulting in an overestimate of low curvatures and underestimate of high curvatures. Without the knowledge of the true curvature distribution, which is the case in the analysis of the experimental data, the correct number of modes is difficult to determine *a priori*. We therefore conclude that this method is of limited value for determining the curvature distribution for unknown conditions in living cells.

We also investigated using polynomials or sine transforms for fitting shapes. We found a similar problem with using polynomials because an optimal order for the polynomial needs to be determined, and this order depends on the shape of each polymer. In addition, the polynomial method has problems measuring the curvature at the ends of the polymers due to poor fitting. The sine transform also has difficulty matching the shape at the ends due to the fact that sine functions do not match the angles at the ends. This edge effect, also known as ringing, is magnified when taking the derivative of the Fourier transform to obtain the curvature. We therefore recommend not using shape-fitting approaches to determine the curvature distribution, especially if: (1) additional nonthermal forces act on the microtubules or (2) the flexural rigidity is not known *a priori*.

VII. Discussion

The results given in this chapter have all been obtained using thermally driven polymer simulation data, and it remains unclear whether *in vivo* data would yield similar results. The shape of the curvature distribution for a thermally driven polymer is Gaussian. Therefore, estimating the curvature distribution serves as an important tool to determine whether the polymer is only subject to thermal forces. If the estimated curvature distribution from a cell is not Gaussian in shape, then the associated bending must be influenced by other factors such as molecular motors, polymerization forces, or actomyosin contractility. However, if the shape is Gaussian, it is still possible that nonthermal sources of bending contribute to the curvature distribution.

For systems where the curvature distribution is not Gaussian, alternative scenarios can be investigated in the framework provided by hybrid SRD-MD simulations. In particular, the effect of molecular motors, elastic forces in the surrounding cytoplasm, polymerization forces, as well as hydrodynamic effects due to the presence of other microtubules can be investigated using this approach. Furthermore, by comparing the experimental curvature distribution with the simulated distribution, we can potentially identify and eliminate models for microtubule bending.

Using shape-fitting methods for estimating curvature distributions may lead to large discrepancies. In particular, results obtained using Fourier cosine transforms depend sensitively on the number of modes used, even for data that is not coarse-grained. In addition, both sine transforms and polynomial methods suffer from end effects. All shape-fitting methods effectively interpolate between the nodes, which results in spurious curvature values in the curvature distribution. We therefore do not recommend the use of fitting functions for estimating the curvature distribution. By comparison, the three-point method is capable of producing a model-independent curvature distribution and is therefore a suitable method for estimating the curvature distributions in living cells.

For noisy data, coarse-graining is necessary in order to prevent digitization and measurement errors from dominating the curvature distribution. The disadvantage of coarse-graining is that the correct variance is lost due to smoothing. However, the curvature distribution still allows for comparison between different experiments, assuming the data collection is done at the same coarse-graining level.

When collecting data from living cells, the position and curvature at the microtubule's ends are not easy to determine. This is due in part to a limited field of view in the microscope, as well as high density of microtubules in the cell body. Even if the microtubules could be traced back to the centrosome, it is still unclear as to whether the ends are clamped or hinged. This is another reason we believe it is necessary to use a local curvature estimation method, such as the three-point method, when analyzing data in living cells.

Our investigation has allowed us to identify a number of important considerations for data collection. First, the minimum spacing between data points along microtubules is important and it should be determined experimentally. Second,

the errors associated with digitization can be large, especially when the image pixel size is larger than the diameter of the microtubule. This error could be reduced by using higher magnification to project the microtubule image over more pixels, effectively reducing the pixel size in the image. However, this will reduce the signal to noise, which will then require one to increase the exposure time or to average over more data points. Perhaps a better approach would be to estimate the microtubule position to subpixel precision, which could be done through the use of a semiautomated method.

VIII. Conclusions

Given an experimental set of discrete coordinates collected from images of microtubules, the first question to be asked is whether the data can be explained by applying a theoretical model. The simplest approach is to assume that thermal forces dominate and use a thermally driven polymer model. To check this hypothesis, we suggest using the three-point method as described in [Section V.A](#) to estimate the curvature distribution, making sure the data collection is done at the appropriate coarse-graining interval. Then, if the estimated curvature distribution is Gaussian in shape, one can interpret the results using a thermal model.

More likely, the bending of microtubules in living cells involves additional nonthermal forces, otherwise one would have to assume that they are much less rigid *in vivo* to match the observed bending. The three-point method provides a simple approach for estimating the curvature of microtubules, independent of the forces that influence bending. The difference in curvature distributions between experiments at similar coarse-graining intervals may then be used as a tool to provide insight into how different cellular processes affect curvature. We believe this approach will complement the existing techniques for investigating microtubule deformation and could potentially turn microtubules into intracellular force transducers.

In order to use microtubules as force transducers, it is important to have an accurate measure of the flexural rigidity *in vivo*. Since the flexural rigidity of microtubules *in vivo* is to the best of our knowledge unknown, one could try for a more realistic “*in vivo*” estimate of EI by using cell extracts. Assuming that forces attributed to molecular motors can be silenced, then one could use any of the methods referenced in [Section II](#) to estimate flexural rigidity from cell extracts. Once EI is known, the deformation of the microtubules, as measured by the curvature distribution can, in principle, be used to estimate the distribution of loads on these microtubules.

Acknowledgments

We thank Dr. Patricia Wadsworth, University of Massachusetts Amherst for kindly supplying us the LLC-PK1- α cell line.

D.M.K. and E.T. acknowledge support from the National Science Foundation under Grant No. DMR-0513393 and ND EPSCoR through NSF grant EPS-0132289. D.J.O. acknowledges support from NSF grants BES 9984955, BES 0119481, and NIGMS R01GM71522.

References

- Arfken, G. B., and Weber, H. J. (2001). "Mathematical Methods for Physicists." Academic Press, San Diego.
- Brangwynne, C. P., Mackintosh, F. C., Kumar, S., Geisse, N. A., Talbot, J., Mahadevan, L., Parker, K. K., Ingber, D. E., and Weitz, D. A. (2006). Microtubules can bear enhanced compressive loads in living cells because of lateral reinforcement. *J. Cell Biol.* **173**(5), 733–741.
- Cassimeris, L., Gard, D., Tran, P. T., and Erickson, H. P. (2001). XMAP215 is a long thin molecule that does not increase microtubule stiffness. *J. Cell Sci.* **114**, 3025–3033.
- Doi, M., and Edwards, S. F. (2004). "The Theory of Polymer Dynamics." Oxford University Press, Oxford.
- De Gennes, P. G. (1979). "Scaling Concepts in Polymer Physics." Cornell University Press, Ithaca, New York.
- Desai, A., and Mitchison, T. J. (1997). Microtubule polymerization dynamics. *Annu. Rev. Cell Dev. Biol.* **13**, 83–117.
- Dogterom, M., and Yurke, B. (1997). Measurement of the force-velocity relation for growing microtubules. *Science* **278**, 856–860.
- Falck, E., Lahtinen, J. M., Vattulainen, I., and Ala-Nissila, T. (2004). Influence of hydrodynamics on many-particle diffusion in 2D colloidal suspensions. *Eur. Phys. J. E* **13**, 267–275.
- Falck, E., Punkkinen, O., Vattulainen, I., and Ala-Nissila, T. (2003). Dynamics and scaling of 2D polymers in a dilute solution. *Phys. Rev. E* **68**, 050102(R).
- Felgner, H., Frank, R., Biernat, J., Mandelkow, E. M., Mandelkow, E., Ludin, B., Matus, A., and Schliwa, M. (1997). Domains of neuronal microtubule-associated proteins and flexural rigidity of microtubules. *J. Cell Biol.* **138**, 1067–1075.
- Felgner, H., Frank, R., and Schliwa, M. (1996). Flexural rigidity of microtubules measured with the use of optical tweezers. *J. Cell Sci.* **109**, 509–516.
- Frenkel, D., and Smit, B. (2002). "Understanding Molecular Simulation. From Algorithms to Applications." Academic Press, Boston.
- Fygenson, D. K., Elbaum, M., Shraiman, B., and Libchaber, A. (1997). Microtubules and vesicles under controlled tension. *Phys. Rev. E* **55**, 850–859.
- Gildersleeve, R. F., Cross, A. R., Cullen, K. E., Fagen, A. P., and Williams, R. C., Jr. (1992). Microtubules grow and shorten at intrinsically variable rates. *J. Biol. Chem.* **267**(12), 7995–8006.
- Gittes, F., Mickey, B., Nettleton, J., and Howard, J. (1993). Flexural rigidity of microtubules and actin filaments measured from thermal fluctuations in shape. *J. Cell Biol.* **120**(4), 923–934.
- Gupton, S. L., Salmon, W. C., and Waterman-Storer, C. M. (2002). Converging populations of F-actin promote breakage of associated microtubules to spatially regulate microtubule turnover in migrating cells. *Curr. Biol.* **12**, 1891–1899.
- Hecht, M., Harting, J., Ihle, T., and Herrmann, H. J. (2005). Simulation of claylike colloids. *Phys. Rev. E* **78**, 011408.
- Heidemann, S. R., Kaech, S., Buxbaum, R. E., and Matus, A. (1999). Direct observations of the mechanical behavior of the cytoskeleton in living fibroblasts. *J. Cell Biol.* **145**, 109–122.
- Howard, J. (2001). "Mechanics of Motor Proteins and the Cytoskeleton." Sinauer Associates, Sunderland, MA.
- Ihle, T., and Kroll, D. M. (2001). Stochastic rotation dynamics: A Galilean-invariant mesoscopic model for fluid flow. *Phys. Rev. E* **63**, 020201(R).
- Ihle, T., and Kroll, D. M. (2003a). Stochastic rotation dynamics. I. Formalism, galilean invariance, and green-kubo relations. *Phys. Rev. E* **67**, 066705.

- Ihle, T., and Kroll, D. M. (2003b). Stochastic rotation dynamics. II. Transport coefficients, numerics, and long-time tails. *Phys. Rev. E* **67**, 066706.
- Ihle, T., Tüzel, E., and Kroll, D. M. (2004). Resummed Green-Kubo relations for a fluctuating fluid-particle model. *Phys. Rev. E* **70**, 035701(R).
- Ihle, T., Tüzel, E., and Kroll, D. M. (2005). Equilibrium calculation of transport coefficients for a fluid-particle model. *Phys. Rev. E* **72**, 046707.
- Janson, M. E., De Dood, M. E., and Dogterom, M. (2003). Dynamic instability of microtubules is regulated by force. *J. Cell Biol.* **161**(6), 1029–1034.
- Janson, M. E., and Dogterom, M. (2004). A bending mode analysis for growing microtubules: Evidence for a velocity-dependent rigidity. *Biophys. J.* **87**, 2723–2736.
- Kaverina, I., Krylyshkina, O., Beningo, K., Anderson, K., Wang, Y. L., and Small, J. V. (2002). Tensile stress stimulates microtubule outgrowth in living cells. *J. Cell Sci.* **115**(11), 2283–2291.
- Kikuchi, N., Gent, A., and Yeomans, J. M. (2002). Polymer collapse in the presence of hydrodynamic interactions. *Eur. Phys. J. E* **9**, 63–66.
- Kirschner, M., and Mitchison, T. (1986). Beyond self-assembly: From microtubules to morphogenesis. *Cell* **45**, 329–342.
- Kis, A., Kasas, S., Babic, B., Kulik, A. J., Benoit, W., Briggs, G. A. D., Schonenberger, C., Catsicas, S., and Forro, L. (2002). Nanomechanics of microtubules. *Phys. Rev. Lett.* **89**, 248101.
- Klapper, I., and Qian, H. (1998). Remarks on discrete and continuous large-scale models of DNA dynamics. *Biophys. J.* **74**, 2504–2514.
- Kurachi, M., Hoshi, M., and Tashiro, H. (1995). Buckling of a single microtubule by optical trapping forces—direct measurement of microtubule rigidity. *Cell Motil. Cytoskeleton* **30**, 221–228.
- Kurz, J. C., and Williams, R. C. (1995). Microtubule-associated proteins and the flexibility of microtubules. *Biochemistry* **34**, 13374–13380.
- Malevanets, A., and Kapral, R. (1999). Mesoscopic model for solvent dynamics. *J. Chem. Phys.* **110**, 8605–8613.
- Malevanets, A., and Kapral, R. (2000). Solute molecular dynamics in a mesoscale solvent. *J. Chem. Phys.* **112**, 7260–7269.
- Malevanets, A., and Yeomans, J. M. (2000). Dynamics of short polymer chains in solution. *Europhys. Lett.* **52**, 231–236.
- Marenduzzo, D., Micheletti, C., Seyed-allaei, H., Trovato, A., and Maritan, A. (2005). Continuum model for polymers with finite thickness. *J. Phys. A: Math. Gen.* **38**, L277–L283.
- Mickey, B., and Howard, J. (1995). Rigidity of microtubules is increased by stabilizing agents. *J. Cell Biol.* **130**, 909–917.
- Mitchison, T., and Kirschner, M. (1984). Dynamic instability of microtubule growth. *Nature* **312**, 237–242.
- Noguchi, H., and Gompper, G. (2004). Fluid vesicles with viscous membranes in shear flow. *Phys. Rev. Lett.* **93**, 258102.
- Odde, D. J., Ma, L., Briggs, A. H., DeMarco, A., and Kirschner, M. W. (1999). Microtubule bending and breaking in living fibroblast cells. *J. Cell Sci.* **112**, 3283–3288.
- Ott, A., Magnasco, M., Simon, A., and Libchaber, A. (1993). Measurement of the persistence length of polymerized actin using fluorescence microscopy. *Phys. Rev. E* **48**(3), R1642–R1645.
- Padding, J. T., and Louis, A. A. (2004). Hydrodynamic and Brownian fluctuations in sedimenting suspensions. *Phys. Rev. Lett.* **93**, 220601.
- Putnam, A. J., Cunningham, J. J., Dennis, R. G., Linderman, J. J., and Mooney, D. J. (1998). Microtubule assembly is regulated by externally applied strain in cultured smooth muscle cells. *J. Cell Sci.* **111**, 3379–3387.
- Press, W. H., Flannery, B. P., Teukolsky, S. A., and Vetterling, W. T. (1992). “Numerical Recipes in C: The Art of Scientific Computing,” 2nd edn. Cambridge University Press, New York.
- Ripoll, M., Mussawisade, K., Winkler, R. G., and Gompper, G. (2004). Low-Reynolds-number hydrodynamics of complex fluids by multi-particle-collision dynamics. *Europhys. Lett.* **68**, 106–112.

- Rusan, N. M., Fagerstrom, C. J., Yvon, A. M., and Wadsworth, P. (2001). Cell cycle dependent changes in microtubule dynamics in living cells expressing green fluorescent protein-alpha tubulin. *Mol. Biol. Cell* **12**(4), 971–980.
- Sprague, B. L., Pearson, C. G., Maddox, P. S., Bloom, K. S., Salmon, E. D., and Odde, D. J. (2003). Mechanisms of microtubule-based kinetochore positioning in the yeast metaphase spindle. *Biophys. J.* **84**(6), 3529–3546.
- Storm, C., Pastore, J. J., MacKintosh, F. C., Lubensky, T. C., and Janmey, P. A. (2005). Non-linear elasticity in biofilament gels. *Nature* **435**, 191–196.
- Takasone, T., Juodkazis, S., Kawagishi, Y., Yamaguchi, A., Matsuo, S., Sakakibara, H., Nakayama, H., and Misawa, H. (2002). Flexural rigidity of a single microtubule. *Jpn. J. Appl. Phys.* **41**, 3015–3019.
- Tüzel, E., Strauss, M., Ihle, T., and Kroll, D. M. (2003). Transport coefficients for stochastic rotation dynamics in three dimensions. *Phys. Rev. E* **68**, 036701.
- Tüzel, E., Ihle, T., and Kroll, D. M. (2006). Dynamic correlations in stochastic rotation dynamics. Pre-print, <http://lanl.arxiv.org/cond-mat/0606628>.
- Van Noort, J., van der Heijden, T., de Jager, M., Wyman, C., Kanaar, R., and Dekker, C. (2003). The coiled-coil of the human Rad50 DNA repair protein contains specific segments of increased flexibility. *Proc. Natl. Acad. Sci. USA* **100**(13), 7581–7586.
- Venier, P., Maggs, A. C., Carlier, M.-F., and Pantaloni, D. (1994). Analysis of microtubule rigidity using hydrodynamic flow and thermal fluctuations. *J. Biol. Chem.* **269**(18), 13353–13360.
- Waterman-Storer, C. M., and Salmon, E. D. (1997). Actomyosin-based retrograde flow of microtubules in the lamella of migrating epithelial cells influences microtubule dynamic instability and turnover and is associated with microtubule breakage and treadmilling. *J. Cell Biol.* **139**, 417–434.
- Winkler, R. G., Mussawisade, K., Ripoll, M., and Gompper, G. (2004). Rod-like colloids and polymers in shear flow: A multi-particle-collision dynamics study. *J. Phys.: Condens. Matter* **16**, 3941–3954.
- Zheng, J., Buxbaum, R. E., and Heidemann, S. R. (1993). Investigation of microtubule assembly and organization accompanying tension-induced neurite initiation. *J. Cell Sci.* **104**(4), 1239–1250.